nature materials

LETTERS

https://doi.org/10.1038/s41563-021-01019-x

Check for updates

# Local electronic structure variation resulting in Li 'filament' formation within solid electrolytes

Xiaoming Liu[1,8], Regina Garcia-Mendez[2,8], Andrew R. Lupini[1], Yongqiang Cheng[3], Zachary D. Hood[4], Fudong Han[5], Asma Sharafi[2], Juan Carlos Idrobo[1], Nancy J. Dudney[6], Chunsheng Wang[5], Cheng Ma[7]✉, Jeff Sakamoto[2]✉ and Miaofang Chi[1]✉

**Solid electrolytes hold great promise for enabling the use of Li metal anodes. The main problem is that during cycling, Li can infiltrate along grain boundaries and cause short circuits, resulting in potentially catastrophic battery failure. At present, this phenomenon is not well understood. Here, through electron microscopy measurements on a representative system, $Li_7La_3Zr_2O_{12}$, we discover that Li infiltration in solid oxide electrolytes is strongly associated with local electronic band structure. About half of the $Li_7La_3Zr_2O_{12}$ grain boundaries were found to have a reduced bandgap, around 1–3 eV, making them potential channels for leakage current. Instead of combining with electrons at the cathode, $Li^+$ ions are hence prematurely reduced by electrons at grain boundaries, forming local Li filaments. The eventual interconnection of these filaments results in a short circuit. Our discovery reveals that the grain-boundary electronic conductivity must be a primary concern for optimization in future solid-state battery design.**

Despite the highest theoretical capacity (3,860 mAh $g^{-1}$) and lowest potential (0 V versus $Li/Li^+$) for Li batteries[1–4], Li metal anodes are presently unsuitable for realizing safe, energy-dense all-solid-state batteries, because solid electrolytes cannot suppress Li dendrite growth and the associated short circuiting during repeated cycling[5–9]. A typical example is cubic $Li_7La_3Zr_2O_{12}$ (LLZO), one of the most promising oxide solid electrolytes. It forms a stable interphase with Li (refs. [10–14]) and is 20 times stiffer than Li (refs. [15–17]). Regardless, once cycled above a critical current density (CCD), Li dendrites penetrate LLZO along its grain boundaries (GBs), causing short circuiting[6,8,18,19]. Presently, the reported CCD values are too low to realize acceptable cell performance. To address the dendrite issue, a thorough understanding of its microscopic origin is indispensable.

However, why Li dendrites could preferentially form along GBs remains unclear. Existing studies are primarily based on the assumption that Li filaments initiate at the LLZO/Li interface[4,5,20–25]. When Porz et al. found that even single-crystalline LLZO cannot prevent Li penetration, pre-existing surface flaws were considered to be responsible for Li filament growth at LLZO/Li interfaces[5]. Tsai et al. proposed that the inhomogeneous Li/solid-electrolyte contact favours uneven Li deposition[25]. In such studies, the non-uniform current distribution at the Li/solid-electrolyte interface is believed to be crucial to Li dendrite formation[4,23,25,26]. By contrast, Han et al. recently reported that the high electronic conductivity of LLZO itself is responsible for dendrite formation[4], but this study is based on macroscopic characterizations, which cannot easily isolate the role of the GBs. A recent theoretical work found that LLZO {110} surfaces present a narrowed bandgap of ~2.1 eV, which could be related to Li dendrite formation[27]. GBs in real materials are often interfaces of two randomly oriented grains and cannot be exclusively composed of {110} surfaces. Systematically investigating such GBs through calculations alone is quite challenging. Consequently, the reason for the preferential dendrite formation along LLZO GBs remains elusive. Further, the assumption that Li filament growth exclusively initiates at the anode is not necessarily valid. Recently, first-principles calculations have indicated that LLZO GBs may favour Li nucleation by themselves[28]. In other words, Li dendrites may not exclusively initiate at LLZO/Li interfaces. To reach a conclusive understanding, two questions have to be answered: (1) How do GB Li filaments initiate and propagate during cycling? (2) Which specific characteristics of GBs enable this process?

Resolving these questions is challenging, because it demands both adequate spatial resolution and the capability of real-time observation. In this study, we provide answers to both questions by combining several advanced electron microscopy techniques with in situ transmission electron microscopy (TEM). One of the most appealing solid electrolytes, LLZO, was selected for study. We discover that Li plating can initiate within the solid electrolyte, following a fundamentally different mechanism from those in the literature. This particular mechanism arises from a largely overlooked behaviour: the local reduction of GB band gaps, which was found to be unprecedentedly severe in some LLZO GBs.

Our high-resolution TEM (HRTEM) results (Fig. 1a and Supplementary Fig. 1) reveal that most grains are directly connected through GBs, that is, free of secondary or amorphous phases. Electron energy loss spectroscopy (EELS) identified minor differences in the fine structures of the O-K and Li-K edges between GBs and the bulk (Fig. 1b,c). For example, the first peak in the Li-K edge is slightly higher, about 11% integrated over the range of 60–67.1 eV, in the bulk spectrum compared to that of the GB. These changes suggest some difference in the bonding environments of the Li and O at the boundaries. While the details of EELS peak shapes in

[1]Center for Nanophase Materials Sciences, Oak Ridge National Laboratory, Oak Ridge, TN, USA. [2]Department of Materials Science and Engineering, University of Michigan, Ann Arbor, MI, USA. [3]Neutron Scattering Division, Oak Ridge National Laboratory, Oak Ridge, TN, USA. [4]School of Chemistry and Biochemistry, Georgia Institute of Technology, Atlanta, GA, USA. [5]Department of Chemical and Bimolecular Engineering, University of Maryland, College Park, MD, USA. [6]Chemical Sciences Division, Oak Ridge National Laboratory, Oak Ridge, TN, USA. [7]Hefei National Laboratory for Physical Sciences at the Microscale, Department of Materials Science and Engineering, CAS Key Laboratory of Materials for Energy Conversion, University of Science and Technology of China, Hefei, China. [8]These authors contributed equally: Xiaoming Liu, Regina Garcia-Mendez. ✉e-mail: mach16@ustc.edu.cn; jeffsaka@umich.edu; chim@ornl.gov

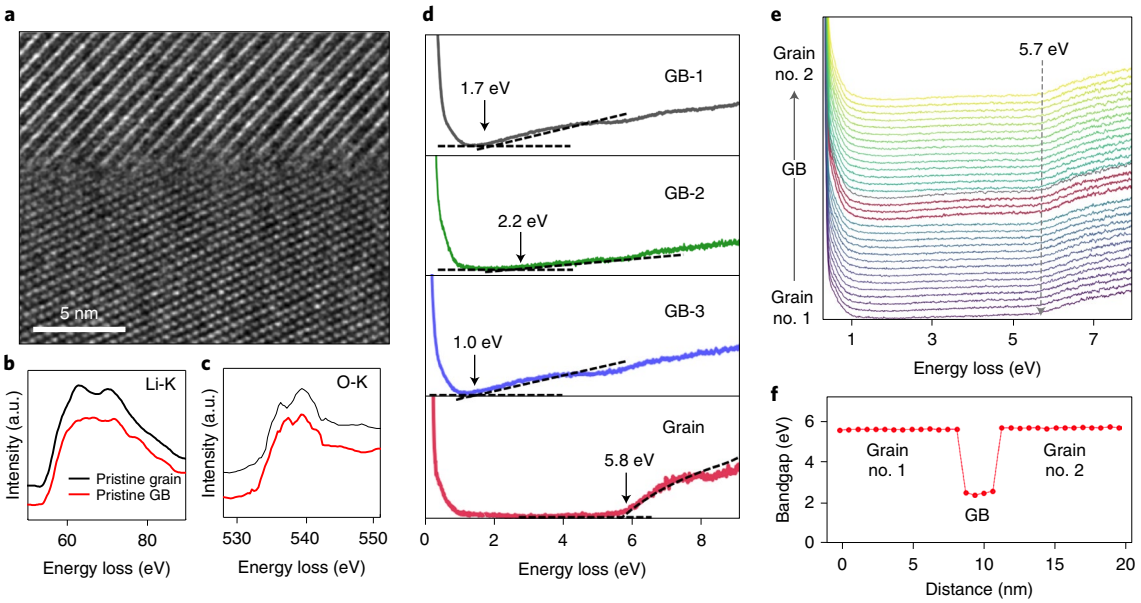


**Fig. 1 | Atomic and electronic structure difference at the grain bulk and GBs of pristine LLZO. a**, HRTEM at a representative GB of pristine LLZO. **b**,**c**, EELS spectra of Li-K edge (**b**) and O-K edge (**c**). **d**, Bandgap measurements at the grain bulk and three GBs. **e**, Line-scan EELS analysis across a typical GB; spectra that involve GB contributions are highlighted in red. **f**, The corresponding bandgap values.

complicated structures are difficult to interpret, local bandgap measurements using valence-EELS deliver a clearer message.

The valence region of an EELS spectrum represents the energy loss caused by the excitation of valence electrons to the conduction band, and the lowest of such energy losses corresponds to the band gap[29–31]. As shown in Fig. 1d, such measurement suggests that the band gap of bulk LLZO is ~6.0 eV, agreeing well with both theoretical calculation and electrochemical characterization[32]. Owing to the large grain size of sintered LLZO pellets, which is ~15.6 ± 9.7 μm, based on scanning electron microscopy (SEM) and electron backscatter diffraction measurements, on average only one or two GBs in each TEM specimen are sufficiently thin for valence-EELS analysis examinations, limiting a larger-scale statistical analysis. Sixteen GBs in total were measured from twelve TEM specimens. Around half of them show a bandgap similar to that of a grain, that is, ~6 eV, while the other half show a reduced band gap that varies from 1 to 3 eV. Typical line-scan valence-EELS across representative GBs and their calculated bandgap values are plotted in Fig. 1e and Supplementary Fig. 2. Methods for bandgap determinations are shown in Supplementary Fig. 3. Reduced band gaps at GBs indicate that these GBs are much poorer electronic insulators than bulk LLZO. Should leakage current occur, the electrons would preferably flow through such GBs.

Potential causes of these reduced band gaps were investigated by examining the structure and chemistry of GBs and comparing the results with their composing grains. HRTEM imaging (Fig. 1a and Supplementary Fig. 1) shows that the GBs in LLZO are generally narrow (below 1.5 nm) and become slightly wider adjacent to triple junctions. They are structurally asymmetric and mainly consist of randomly orientated grains, consistent with our electron backscatter diffraction analysis (Supplementary Fig. 4). Examining the HRTEM images reveals that most of the GB surfaces are complex high-index surfaces, rather than low-energy {110} or {100} surfaces (Supplementary Fig. 5). Taken together, these GB features reveal two important findings: that the atomic structures of different GBs vary greatly, and that the atomic configurations of most GBs, including both atomic arrangements and ionic coordination, deviate from that of LLZO bulk. These findings are important because deviations in atomic structure and coordination often lead to modifications in the local electronic structure, as reported in previous theoretical studies of small-angle GBs and surfaces of LLZO[27,28].

Modified electronic structures at GBs could thus be responsible for the changes in the band gaps. Indeed, reduced band gaps at GBs have been reported in other ceramic materials, such as bicrystal $SrTiO_3$, MgO and $Al_2O_3$ (refs. [33–35]). Among these previous reports, the largest bandgap reduction is reported in MgO GBs, with reductions of up to 3 eV (ref. [33]), depending on the specific GB configuration. In our case, the arbitrariness of the constituent surfaces thus most probably contributes to the bandgap variations between the different GBs. The GBs with reduced bandgaps are expected to contain a locally increased number of free charge carriers, potentially giving high local electronic conductivities. Experimental measurements of the electronic conductivity of LLZO are reported to be $10^{-8}$–$10^{-7}$ S cm$^{-1}$ at room temperature in polycrystalline LLZO[4,8,36]. The electronic conductivity of single-crystalline LLZO was recently reported to be about $5 \times 10^{-10}$ S cm$^{-1}$ at 293 K (ref. [37]). These results suggest that the conductivity could be increased by several orders of magnitude owing to the presence of GBs.

In reality, GBs with a reduced bandgap are not always connected to each other to form a channel throughout the electrolyte pellet. Another noteworthy fact is the magnitude of the bandgap reduction observed in some GBs. Although the large bandgap reduction is unambiguously demonstrated by our direct observation and is consistent with the aforementioned distinction between single-crystal and polycrystalline materials, some LLZO GBs were observed to undergo more severe bandgap reduction (up to 5 eV), which is larger than previously reported in other oxides[33–35]. Whereas the present study intends to focus only on the mechanism of Li dendrite growth, the remarkable magnitude of the bandgap reduction in these particular GBs also deserves future in-depth investigation.

To identify potential causes of this variation in addition to local GB atomic configurations, the local chemistries of the GBs were studied by using EELS and energy dispersive X-ray spectroscopy (EDX), which did not reveal obvious changes in the Li, La, Al or Zr, although a subtle reduction of O concentration was sometimes seen (Supplementary Fig. 6). A value of ~2 atomic per cent is estimated

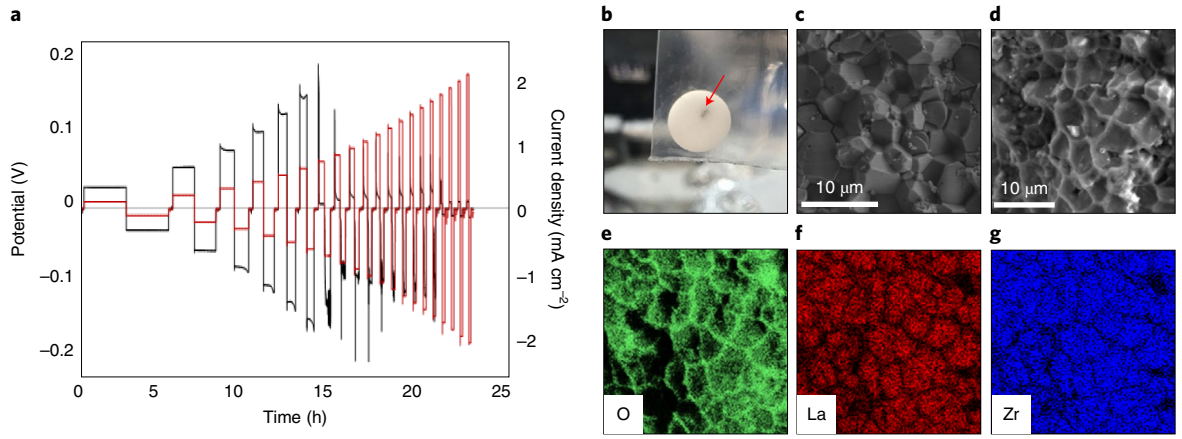


**Fig. 2 | The d.c. cycling test of LLZO and microscopy images of LLZO after dendrite penetration. a**, The d.c. cycling of Li/LLZO/Li cells at room temperature, stepping the current density from 0.01 to 2 mA cm$^{-2}$. The black and red curves correspond to the potential and current density, respectively. **b**, Optical microscopy image of a cycled LLZO pellet. The black spot highlighted by the arrow is the region where the short circuit occurred. **c**, SEM image of the pristine LLZO in a cross-section. **d**, SEM image of the cycled LLZO at the short-circuit region, showing a web structure along the GBs. **e**–**g**, Elemental EDX mapping of O, La and Zr, respectively.

by comparing integrated O-K edges from the spectra, indicating the presence of a small number of oxygen vacancies at GBs. These oxygen vacancies may induce defect states within the bandgap and move the band edges; an example is shown in Supplementary Fig. 7. In a real LLZO GB, where the structure and chemistry are much more complicated, a variety of defects, along with structural/chemical disorder, are present and can result in an effectively reduced bandgap, as observed by EELS. These defects could be oxygen vacancies at different lattice sites or with different concentrations; structural and chemical fluctuations; and/or the presence of other elemental defects or impurities, for example trace carbon impurity atoms, all of which may contribute to the narrowed bandgaps. These details merit future investigation. Regardless of the origin, the bandgap reduction at LLZO GBs is clear, and its connection with the preferential dendrite formation needs to be determined.

The LLZO pellet was further examined after it was cycled as a Li/LLZO/Li cell under galvanostatic conditions until the CCD was exceeded. The CCD was found to be 0.7 mA cm$^{-2}$ at room temperature (Fig. 2a). This pellet showed a dark spot at its surface (Fig. 2b). This represents the location where Li infiltrated the solid electrolyte and caused the short circuit[6]. Cross-sections of specimens along the short-circuited regions were used to characterize the Li dendrite network using SEM. In contrast to the GBs in pristine LLZO (Fig. 2c), the cycled LLZO contained GB secondary phases (Fig. 2d) that percolate through the GB network. To provide image contrast, cycled samples were intentionally exposed to air for five seconds to form $Li_xO$ and $Li_2CO_3$. EDX mapping (Fig. 2e–g) indicates that the GB second phase contains negligible concentrations of La and Zr, but is O rich, further suggesting the presence of $Li_2O$, formed from exposure to air—results consistent with previous studies[6].

At this point, we have learned two relevant facts: (1) When the current density is large enough to reduce the GB potential below 0 V, GBs will serve as the channels for Li deposition. (2) The continuous Li deposition and growth along GBs will eventually cause short circuiting. Aligning these two aspects leads to our hypothesis: at a sufficiently large current density, it could be that the electrons in the GB leakage current decrease the local potential sufficiently to reduce $Li^+$ into Li metal, leading to filament formation along GBs. If correct, Li infiltration into the solid electrolyte, unlike the case for liquid electrolytes, does not necessarily occur at the Li/solid-electrolyte interface during Li plating. Instead, Li filaments could initiate independently at GBs with relatively large electron flows, and then gradually grow during cycling. The short circuit would result from the eventual interconnection among these growing (but originally isolated) Li filaments, rather than exclusively directional growth from the Li anode towards the cathode. Since this process requires only the presence of electrons at GBs, it may take place when the local potential is below 0 eV. Consequently, the direct observation of Li filament formation under Li ion flow would be vital to the verification of our hypothesis.

Here, in situ TEM was performed using a set-up similar to our previous study (Supplementary Fig. 8)[38]. During observations, Li was driven towards LLZO to form an in situ contact, and then a bias with the direction indicated in Supplementary Fig. 8 was applied to trigger Li flow. In this configuration, as LLZO is mounted on a copper grid, at the initial bias, $Li^+$ is expected to travel from the Li metal towards the copper and deposit at the LLZO/Cu interface, forming a Li/LLZO/Li symmetric cell. Figure 3a shows the bright-field TEM image of the region selected for study, where three GBs were connected with a void at the triple junction. A triple junction with

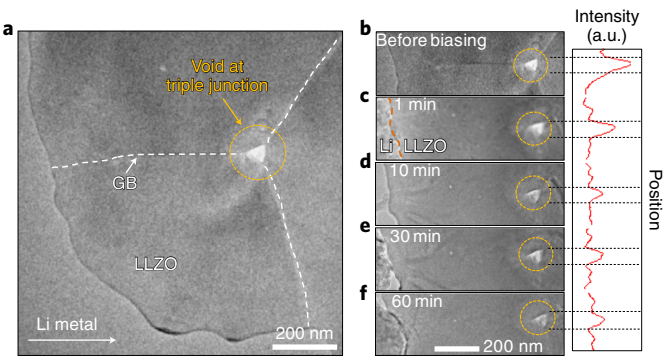


**Fig. 3 | In situ TEM observation of the LLZO GB during biasing. a**,**b**, Pristine LLZO before touching with Li metal. The GB is highlighted by white dashed lines, while the void at the triple junction is circled with a dashed orange line. **c**–**f**, LLZO biased using Li metal electrodes at 10 V for 1, 10, 30 and 60 min, respectively. The red dashed line in **c** delineates the interface between Li and LLZO. The plot of the brightness intensity at the void region in panels **b** through **f** is presented correspondingly on the right. The decrease of the brightness is caused by the filling of Li into voids during biasing.

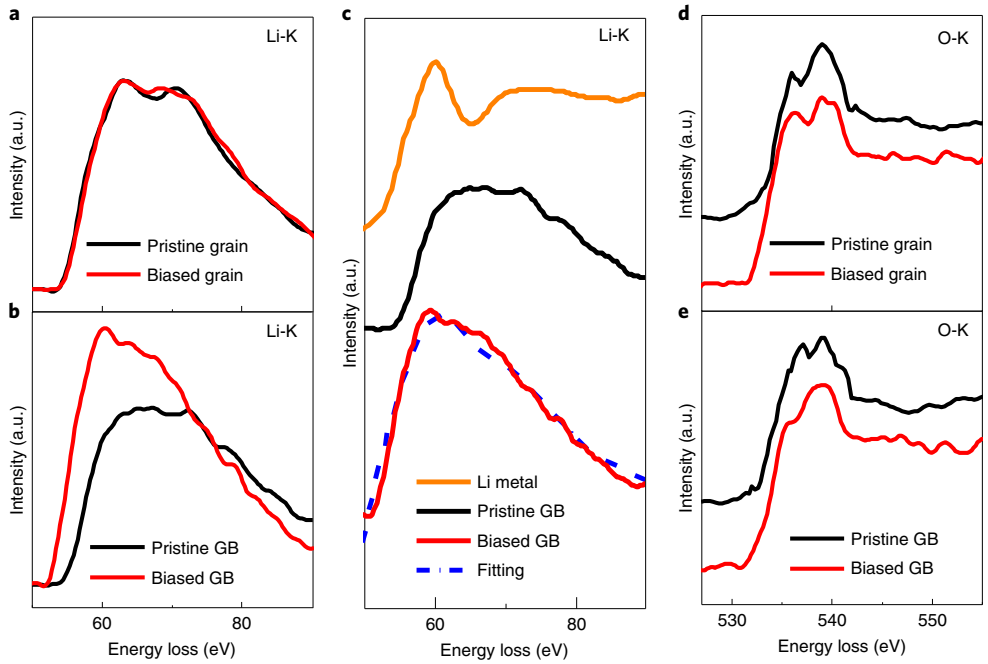


**Fig. 4 | The structure and chemistry evolution at the grain bulk and GB during biasing. a**,**b**, EELS spectra of Li-K edge. The intensity is normalized to that of the La $N_{4,5}$ edge. The Li concentration increased by 25% at the GB after biasing. **c**, EELS spectra of Li-K edge. The dashed curve indicates the multiple linear least-squares fitting, showing the Li-K edge at the biased GB is a linear combination of Li-K edges between Li metal and pristine GB. **d**,**e**, EELS spectra of the O-K edges. The intensity is normalized to the maximum of the O-K edges. The EELS spectrum measurements of the grain bulk were collected at least 100 nm away from the surface.

a relatively large void was intentionally chosen in order to clearly observe the Li plating. Although the changes in the GB itself cannot be easily revealed in TEM, contrast changes in the triple junction can serve as an indicator of Li plating at GBs as the lithium metal is depleted from the junction as a directional high voltage is applied. Figure 3b–f shows the intensity change in the triple-junction void when an electrical bias of 10 V was applied. The image intensity at the void gradually weakens to a level comparable with the surrounding grains as a function of time. The brightness decrease occurred first near the GBs, and then gradually filled the void. Clearly, severe phase segregation at GBs was triggered by external biasing, and the segregated phase flowed into the void. The occurrence of this phenomenon demands a sufficiently large current density; otherwise nothing would happen (Supplementary Fig. 9). This behaviour fits the characteristic of GB Li filament growth: it only took place when cycled beyond the CCD.

EELS analysis supports the conclusion that this newly emerged GB phase is Li metal, and that the grain bulk remains largely unaffected by biasing. As shown in Fig. 4a, neither the intensity nor the fine structure of the Li-K edge in the grain bulk next to the GB experienced any noticeable change after biasing. By contrast, the Li-K edge varied severely at GBs (Fig. 4b). The intensity became much stronger, indicating a dramatic increase in Li content. Furthermore, the Li-K fine structures also evolved towards the characteristics of Li metal. Figure 4c compares the Li-K edges of the biased GB, pristine GB and pure Li metal. Clearly, the spectrum of the biased GB resembles both the pristine GB and Li metal, and thus could result from the linear combination of these two spectra. Multiple linear least squares fitting to the data of the biased GB using those of Li metal and the pristine GB verified this possibility (Fig. 4c). Therefore, we conclude that the biased GB consists of the largely unchanged form from the pristine GB combined with segregated Li metal.

This scenario is also supported by the O-K edges. Although Li metal does not directly contribute to the O-K signal, it has been reported that the O-K prepeak of LLZO would weaken after being contacted with Li (ref. [10]). In the in situ experiments here, while the O-K fine structures of the grain bulk almost remained unchanged after biasing (Fig. 4d), the GB showed an obvious decrease in the O-K prepeak intensity (Fig. 4e). This again confirms that Li segregated along GBs, leaving the grain bulk almost unaffected. Further, since the adjacent grain bulk region, the edge of which was originally in contact with the Li tip, remains intact in both electronic structure and chemistry, the contribution of potential surface diffusion should be rather small. Given that the biasing here was applied in a direction to drive $Li^+$ through LLZO and to deposit it inside LLZO with a Cu grid current collector (Fig. 3 and Supplementary Fig. 8), these in situ observations demonstrate that here, Li filaments preferentially form along GBs during cycling.

Based on the above results, Li infiltration in LLZO solid electrolytes should be regarded as a fundamentally different phenomenon from Li dendrite growth in liquid electrolytes. As schematically illustrated in Fig. 5, local band structure plays a crucial part. With narrow bandgaps, when the local potential at GBs exceeds the bandgaps, LLZO cannot resist electron flows as well as the bulk can. When leakage current occurs, the GBs serve as the source of electrons. As a result, instead of combining with electrons at the cathode, some $Li^+$ ions receive electrons at GBs during cycling, once the local potential is below the reduction potential of $Li/Li^+$, resulting in isolated intergranular Li segregation. The nucleation of Li metal at GBs here thus is locally voltage dependent instead of just current density dependent as conventionally believed. The further growth of this segregated Li will result in Li forming in the GB network and eventually lead to short circuiting. In sharp contrast to Li dendrite growth in liquid electrolytes, this process does not necessarily initiate at the interface between the Li and the solid electrolyte. The eventual short circuit is not caused by the growth of protruding Li towards the cathode, but instead could be caused by the interconnection of the originally isolated Li deposits.

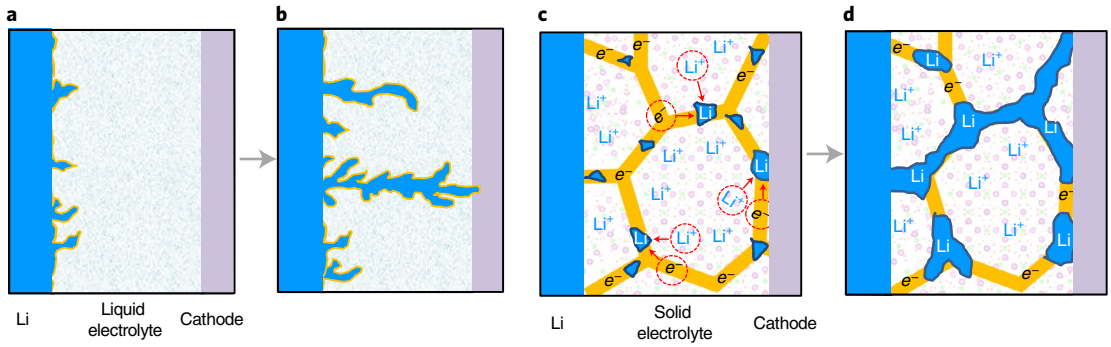


**Fig. 5 | Schematic illustrations. a**,**b**, Conventional dendrite formation and growth in batteries with liquid electrolyte. **c**,**d**, An additional mechanism of filament formation and penetration in solid-state batteries with polycrystalline electrolytes.

The growth of a Li dendrite and its network formation along the GBs may involve multiple factors of GBs, such as the mechanical properties and the dynamically evolving local electric potential, in addition to the presence of 'free' electrons. Given that the term 'dendrite' usually implies a tree-like, directional growth, the segregated Li in solid electrolytes might be more appropriately referred to as 'Li filaments' to distinguish it from the Li dendrite growth in liquid electrolytes. The discovery of this mechanism does not necessarily exclude the simultaneous occurrence of interfacial Li protrusion during Li plating. However, it does suggest that the band structure of GBs must be properly tailored to fully prevent Li infiltration. In addition to the mechanical properties, the presence of surface defects[5] and the existence of an electrochemically unstable secondary phase, wide GB bandgaps should also be ensured, so that electrons cannot easily leak into local GBs and reduce $Li^+$ into Li.

In summary, we provide insight into the microscopic evidence for local electronic band structure affecting Li filament formation in a technologically important solid electrolyte, LLZO. The material is found to undergo a large bandgap reduction at some GBs and, in some cases, the magnitude of this reduction is larger than previously reported for other oxides. This phenomenon initiates the formation of lithium filaments within the solid electrolyte. The final connection of these filaments could result in a short circuit. These insights imply that tailoring GBs with sufficient electronic resistivity will be a promising route towards mitigating Li metal infiltration in polycrystalline solid electrolytes.

## Online content

Any methods, additional references, Nature Research reporting summaries, source data, extended data, supplementary information, acknowledgements, peer review information; details of author contributions and competing interests; and statements of data and code availability are available at https://doi.org/10.1038/s41563-021-01019-x.

Received: 25 December 2018; Accepted: 22 April 2021;
Published online: 31 May 2021

## References

1. Lin, D., Liu, Y. & Cui, Y. Reviving the lithium metal anode for high-energy batteries. *Nat. Nanotechnol.* **12**, 194–206 (2017).
2. Xu, W. et al. Lithium metal anodes for rechargeable batteries. *Energy Environ. Sci.* **7**, 513–537 (2014).
3. Albertus, P., Babinec, S., Litzelman, S. & Newman, A. Status and challenges in enabling the lithium metal electrode for high-energy and low-cost rechargeable batteries. *Nat. Energy* **3**, 16–21 (2018).
4. Han, F. et al. High electronic conductivity as the origin of lithium dendrite formation within solid electrolytes. *Nat. Energy* **4**, 187–196 (2019).
5. Porz, L. et al. Mechanism of lithium metal penetration through inorganic solid electrolytes. *Adv. Energy Mater.* **7**, 1701003 (2017).
6. Ren, Y., Shen, Y., Lin, Y. & Nan, C. W. Direct observation of lithium dendrites inside garnet-type lithium-ion solid electrolyte. *Electrochem. Commun.* **57**, 27–30 (2015).
7. Aguesse, F. et al. Investigating the dendritic growth during full cell cycling of garnet electrolyte in direct contact with Li metal. *ACS Appl. Mater. Interfaces* **9**, 3808–3816 (2017).
8. Cheng, E. J., Sharafi, A. & Sakamoto, J. Intergranular Li metal propagation through polycrystalline $Li_{6.25}Al_{0.25}La_3Zr_2O_{12}$ ceramic electrolyte. *Electrochim. Acta* **223**, 85–91 (2017).
9. Sharafi, A., Meyer, H. M., Nanda, J., Wolfenstine, J. & Sakamoto, J. Characterizing the Li–$Li_7La_3Zr_2O_{12}$ interface stability and kinetics as a function of temperature and current density. *J. Power Sources* **302**, 135–139 (2016).
10. Ma, C. et al. Interfacial stability of Li metal–solid electrolyte elucidated via in situ electron microscopy. *Nano Lett.* **16**, 7030–7036 (2016).
11. Cheng, L. et al. The origin of high electrolyte–electrode interfacial resistances in lithium cells containing garnet type solid electrolytes. *Phys. Chem. Chem. Phys.* **16**, 18294–18300 (2014).
12. Zhu, Y., He, X. & Mo, Y. First principles study on electrochemical and chemical stability of solid electrolyte–electrode interfaces in all-solid-state Li-ion batteries. *J. Mater. Chem. A* **4**, 3253–3266 (2016).
13. Hofstetter, K., Samson, A. J., Narayanan, S. & Thangadurai, V. Present understanding of the stability of Li-stuffed garnets with moisture, carbon dioxide, and metallic lithium. *J. Power Sources* **390**, 297–312 (2018).
14. Li, Y. et al. Garnet electrolyte with an ultralow interfacial resistance for Li-metal batteries. *J. Am. Chem. Soc.* **140**, 6448–6455 (2018).
15. Yu, S. et al. Elastic properties of the solid electrolyte $Li_7La_3Zr_2O_{12}$ (LLZO). *Chem. Mater.* **28**, 197–206 (2016).
16. Ni, J. E., Case, E. D., Sakamoto, J. S., Rangasamy, E. & Wolfenstine, J. B. Room temperature elastic moduli and Vickers hardness of hot-pressed LLZO cubic garnet. *J. Mater. Sci.* **47**, 7978–7985 (2012).
17. Shen, F., Dixit, M. B., Xiao, X. & Hatzell, K. B. Effect of pore connectivity on Li dendrite propagation within LLZO electrolytes observed with synchrotron X-ray tomography. *ACS Energy Lett.* **3**, 1056–1061 (2018).
18. Suzuki, Y. et al. Transparent cubic garnet-type solid electrolyte of $Al_2O_3$-doped $Li_7La_3Zr_2O_{12}$. *Solid State Ion.* **278**, 172–176 (2015).
19. Sudo, R. et al. Interface behavior between garnet-type lithium-conducting solid electrolyte and lithium metal. *Solid State Ion.* **262**, 151–154 (2014).
20. Duan, H., Zheng, H., Zhou, Y., Xu, B. & Liu, H. Stability of garnet-type Li ion conductors: an overview. *Solid State Ion.* **318**, 45–53 (2018).
21. Yang, C. et al. Continuous plating/stripping behavior of solid-state lithium metal anode in a 3D ion-conductive framework. *Proc. Natl Acad. Sci. USA* **115**, 3770–3775 (2018).
22. Wu, B. et al. The role of the solid electrolyte interphase layer in preventing Li dendrite growth in solid-state batteries. *Energy Environ. Sci.* **11**, 1803–1810 (2018).
23. Fu, K. K. et al. Toward garnet electrolyte–based Li metal batteries: an ultrathin, highly effective, artificial solid-state electrolyte/metallic Li interface. *Sci. Adv.* **3**, e1601659 (2017).
24. Sharafi, A. et al. Surface chemistry mechanism of ultra-low interfacial resistance in the solid-state electrolyte $Li_7La_3Zr_2O_{12}$. *Chem. Mater.* **29**, 7961–7968 (2017).
25. Tsai, C. L. et al. $Li_7La_3Zr_2O_{12}$ interface modification for Li dendrite prevention. *ACS Appl. Mater. Interfaces* **8**, 10617–10626 (2016).
26. Wu, B. et al. The role of the solid electrolyte interphase layer in preventing Li dendrite growth in solid-state batteries. *Energy Environ. Sci.* **11**, 1803–1810 (2018).
27. Tian, H. K., Liu, Z., Ji, Y., Chen, L. Q. & Qi, Y. Interfacial electronic properties dictate Li dendrite growth in solid electrolytes. *Chem. Mater.* **31**, 7351–7359 (2019).

28. Yu, S. & Siegel, D. J. Grain boundary contributions to Li-ion transport in the solid electrolyte $Li_7La_3Zr_2O_{12}$ (LLZO). *Chem. Mater.* **29**, 9639–9647 (2017).
29. Hachtel, J. A., Lupini, A. R. & Idrobo, J. C. Exploring the capabilities of monochromated electron energy loss spectroscopy in the infrared regime. *Sci. Rep.* **8**, 5637 (2018).
30. Zhan, W. et al. Nanoscale mapping of optical band gaps using monochromated electron energy loss spectroscopy. *Nanotechnology* **28**, 105703 (2017).
31. Tizei, L. H. G. et al. Exciton mapping at subwavelength scales in two-dimensional materials. *Phys. Rev. Lett.* **114**, 107601 (2015).
32. Thompson, T. et al. Electrochemical window of the Li-ion solid electrolyte $Li_7La_3Zr_2O_{12}$. *ACS Energy Lett.* **2**, 462–468 (2017).
33. Bean, J. J. et al. Atomic structure and electronic properties of MgO grain boundaries in tunnelling magnetoresistive devices. *Sci. Rep.* **7**, 45594 (2017).
34. Chisholm, M. F. et al. Electronic structure of a grain-boundary model in $SrTiO_3$. *Phys. Rev. B* **60**, 2416–2424 (1999).
35. Guhl, H. et al. Structural and electronic properties of Σ7 grain boundaries in $\alpha$-$Al_2O_3$. *Acta Mater.* **99**, 16–28 (2015).
36. Rangasamy, E., Wolfenstine, J. & Sakamoto, J. The role of Al and Li concentration on the formation of cubic garnet solid electrolyte of nominal composition $Li_7La_3Zr_2O_{12}$. *Solid State Ion.* **206**, 28–32 (2012).
37. Knauth, P. Inorganic solid Li ion conductors: an overview. *Solid State Ion.* **180**, 911–916 (2009).
38. Ma, C. et al. Atomic-scale origin of the large grain-boundary resistance in perovskite Li-ion-conducting solid electrolytes. *Energy Environ. Sci.* **7**, 1638–1642 (2014).

## Methods

**LLZO synthesis, processing and surface preparation.** $Li_{6.25}Al_{0.25}La_3Zr_2O_{12}$ solid electrolyte was synthesized from starting powders of $Li_2CO_3$, $Al_2O_3$, $La_2O_3$ and $ZrO_2$ from a solid-state reaction method, calcined at 1,000 °C for 4 h in dry air. Densification of Al–LLZO was achieved by rapid induction hot pressing green bodies of calcined Al–LLZO at 1,225°C and 47 MPa for 40 min in an argon atmosphere with a heating rate of 120.5 °C min$^{-1}$ and cooling rates of 42.5 °C min$^{-1}$ to 800 °C and 22.5 °C min$^{-1}$ to 350 °C. The hot-pressed pellets were cut into 1.5 mm nominal thicknesses using a diamond saw with mineral oil as the cutting fluid. The LLZO hot-pressed discs were ground with a lapping fixture and 400 grit silicon carbide sandpaper onto a glass plate to achieve parallel faces. Further grinding was conducted with 600 and 1,200 grit sandpaper. Polishing and surface preparation to attain low interfacial resistance against Li was done following a previously reported procedure[24], adding a final polishing step of 0.1 µm of diamond polishing abrasive before heat treatment at 400 °C for 3 h in an Ar atmosphere.

**Cell assembly and electrochemical characterization.** A 10 µm nominal thickness of Li was vapour deposited using an Angstrom Engineering deposition system onto laser-cut Kapton masks with an ~32 mm inner diameter. Then 750-µm-thick Li foil discs were placed behind the vapour-deposited Li to avoid Li depletion during stripping, followed by heating the Li symmetric cell at 175 °C under <1 MPa pressure for 12 hours.

Galvanostatic cycling was performed in order to determine the CCD of the samples at room temperature under 4.2 MPa of stack pressure. Current densities were stepped up in 0.1 mA cm$^{-2}$ increments with a fixed charge of 0.25 mAh cm$^{-2}$ for each step. The CCD was determined at the current density when negligible cell potential was measured, coupled with inductive behaviour from a.c. measurements.

**TEM and characterization.** After short circuiting, the cell was disassembled and the LLZO solid electrolyte was collected for SEM examination on the fractured surface using a Hitachi NB5000 focused ion beam (FIB)/SEM microscope. The lamellar LLZO TEM specimen was fabricated using FIB in an FEI Nova microscope. In order to minimize the beam damage in FIB, a protective carbon layer of ~30 nm was deposited on the specimen surface using a 208C Cressington High Vacuum Turbo Carbon Coater prior to FIB experiments. Deposition of further protective layers was performed using the FIB instrument, including an electron-beam-deposited 50 nm carbon layer and an ion-beam-deposited 60 nm W layer.

These protect layers were afterwards removed by ion milling using a Fischione 1010 Ion Mill at −100 °C. A low voltage ion beam with 0.5 kV and 3 mA was used to remove surface damage. For the in situ TEM experiments, the TEM specimen was loaded into a Nanofactory scanning probe TEM holder. The Li metal electrode was prepared by scraping Li foil using a W tool. The exposure of the LLZO sample and Li metal to ambient air was controlled (exposure was <60 seconds).

The STEM imaging, core-loss EELS and EDX analysis were conducted using a JEOL NEOARM equipped with a Gatan Image Filter Quantum-865 and dual Si drift detectors operated at 200 kV. HRTEM images and core-loss EELS were acquired using a Gatan model 636 Liquid Nitrogen Cooling Holder at approximately −170 °C. Core-loss EELS data were collected with a dispersion of 0.2 eV per channel and a collection angle of 30 mrad. The in situ experiments were performed on an FEI Titan S/TEM operated at 300 kV. During in situ studies, the Li-covered W tip was driven onto the LLZO surface using the piezomanipulator on the Nanofactory holder. A series of biases (up to 10 V) was applied on the holder in order to conduct the lithiation process. Real-time observation of the biasing process was recorded under TEM mode.

The bandgap measurements were performed on a Nion aberration-corrected high energy resolution monochromated EELS-STEM operated at 60 kV accelerating voltage. The energy resolution of each single spectrum acquired in this work was ~30 meV with a dispersion of 0.005 eV per channel, measured using the full-width at half-maximum of the zero-loss peak. The low-loss EELS data were acquired with a 1 mm aperture corresponding to a collection angle of about 13 mrad, a probe with a convergence semi-angle of 30 mrad and a beam current of ~10 pA.

**Determination of bandgap values from valence-EELS spectra.** Methods that are used to quantify the bandgap are shown in Supplementary Fig. 2. The bandgaps of spectra acquired from the grain bulk were determined using the procedure reported by Lazar et al.[39]. In this case, for a direct gap, the spectrum intensity ($I_{direct}$) is proportional to the product of the joint density of states (JDOS) and the transition matrix element. Here, the JDOS is given by

$$I_{direct} \propto (E - E_g)^{1/2}$$

Here, $E$ is the energy loss and $E_g$ is the bandgap. The $E_g$ value is defined as the intersection of the fitted curve and a straight line fit to the background.

Unfortunately, the same method is not applicable to the lower energy region of the spectrum, that is, where the intensity due to interstitial states at GBs appears. Instead, the bandgap is defined from the intersection of linear fits to the intensity increase and the background line. This method was reported earlier by Park et al.[40]. As shown in Supplementary Fig. 2, these methods will give very similar results, although the precise values depend on the fitting ranges used. Several different methods are being used for the bandgap determination in the microscopy community, which might result in some variation of the quantitative value assigned to the bandgap. However, the conclusion that bandgaps are reduced at GBs in LLZO does not change.

**Density functional theory calculations.** Modelling by density functional theory of the original and defective cubic-LLZO was performed using the Vienna Ab initio Simulation Package. The calculation used the projector augmented wave method to describe the effects of core electrons. For structural relaxation, Perdew–Burke–Ernzerhof implementation of the generalized gradient approximation for the exchange–correlation functional was used. The energy cut-off was 600 eV for the plane-wave basis of the valence electrons. The relaxed unit cell for the original cubic-LLZO with a lattice constant of 12.975 Å contains 50 Li, 2 Al, 24 La, 16 Zr and 96 O, corresponding to a nominal composition of $Li_{6.25}Al_{0.25}La_3Zr_2O_{12}$. The Li-rich, O-deficient structure contains two O vacancies. The Li, Al and defects were distributed randomly by following these rules: (1) Li occupancy of 24*d* sites is about 0.5, (2) Li occupancy of 96*h* sites is about 0.4 without forming nearest neighbour pairs, and (3) Al occupies 24*d* sites. The electronic structure was calculated on a 2×2×2 Monkhorst–Pack mesh. The total energy tolerance for electronic energy minimization was $10^{-6}$ eV. The maximum interatomic force after relaxation was below 0.02 eV Å$^{-1}$. The relaxed configurations were then taken for more accurate calculation of density of states using the hybrid functional HSE06.

## Data availability

The data that support the findings of this study are available from the corresponding authors upon reasonable request.

## References

39. Lazar, S., Botton, G. A., Wu, M.-Y., Tichelaar, F. D. & Zandbergen, H. W. Materials science applications of HREELS in near edge structure analysis and low-energy loss spectroscopy. *Ultramicroscopy* **96**, 535–546 (2003).
40. Park, J. & Yang, M. Determination of complex dielectric functions at $HfO_2$/Si interface by using STEM-VEELS. *Micron* **40**, 365–369 (2009).

## Acknowledgements

This work was initiated as part of a project supported by the US Department of Energy (DOE), Office of Science, Basic Energy Sciences, Materials Sciences and Engineering Division. Technique developments and M.C.'s efforts on analysis and manuscript preparation were supported by DOE Basic Energy Sciences early career award no. ERKCZ55. Microscopy was conducted at Oak Ridge National Laboratory's Center for Nanophase Materials Sciences, which is a DOE Office of Science User Facility. A.S. and J.S. acknowledge support from the DOE Advanced Battery Material Research programme grant no. DE-EE00006821. Y.C. acknowledges computing resources made available through the VirtuES project, funded by Laboratory Directed Research and Development programme and Compute and Data Environment for Science (CADES). C.M. acknowledges support from the National Key R&D Program of China (2018YFA0209600, 2017YFA0208300), the National Natural Science Foundation of China (51802302) and the Fundamental Research Funds for the Central Universities (WK2060190085, WK3430000006). M.C. thanks R. Erni at ETH Zurich for the valuable discussions on valence-EELS analysis. Part of the research was conducted using instrumentation within ORNL's Materials Characterization Core provided by UT-Batelle under contract no. DE-AC05-00OR22725 with the DOE.

## Author contributions

M.C. conceived the study. X.L. performed the TEM, EELS, SEM and EDX. R.G.-M., A.S. and J.S. performed the LLZO synthesis, electrochemical measurements and electron backscatter diffraction. A.R.L., J.C.I. and M.C. performed the valence-EELS experiments and carried out the related analysis. C.W. and F.H. performed SEM characterizations. Y.C. performed density functional theory calculations. M.C., C.W., C.M., Y.C. and J.S. interpreted the results. C.M. and X.L. wrote the manuscript. All authors contributed to the discussion of the results and the manuscript editing.

## Competing interests

The authors declare no competing interests.

## Additional information

**Supplementary information** The online version contains supplementary material available at https://doi.org/10.1038/s41563-021-01019-x.

**Correspondence and requests for materials** should be addressed to C.M., J.S. or M.C.

**Peer review information** *Nature Materials* thanks the anonymous reviewers for their contribution to the peer review of this work.

**Reprints and permissions information** is available at www.nature.com/reprints.